RSC Advances

ROYAL SOCIETY OF CHEMISTRY

www.rsc.org/advances

Cite this: DOI: 10.1039/c0xx00000x

www.rsc.org/xxxxxx

PAPER

Single Step Synthesis of (α-Fe_2O_3) Hematite Films by Hydrothermal Electrochemical Deposition

Ceren Yilmaz[a] and Uğur Ünal*[a,b,c]

Received (in XXX, XXX) Xth XXXXXXXXX 20XX, Accepted Xth XXXXXXXXX 20XX

DOI: 10.1039/b000000x

A single step electrodeposition of α-Fe_2O_3 films under hydrothermal conditions without post-annealing requirement is described. Primary attention is paid to understand the effects of synthesis conditions such as temperature, precursor concentration, pH and time on the structure and morphology of the films. Moreover, photoelectrochemical properties of hematite films grown by hydrothermal-electrochemical deposition (HED) are also discussed. It is discovered that HED enables production of crystalline α-Fe_2O_3 phase without thermal annealing as opposed to electrodepositions reported at ambient temperature. Photoelectrochemical studies demonstrated that higher performance can be obtained with the films prepared at higher pH. Net photocurrent density of 23.6 $\mu A/cm^2$ is obtained in 0.1 M NaOH under 1 sun conditions at 1.23 V vs NHE with the film prepared from a bath containing 0.05 M $FeCl_2$ and 0.1 M $NaCH_3COOH$ via hydrothermal-electrodeposition with a photocurrent onset potential of 0.96 V vs NHE.

Introduction

There is a strong motivation to prepare ferric oxide nanoparticles of various sizes due to their novel properties and potential applications in medicine, catalysts, magnetic recording media, pigments, anticorrosive agents, gas sensors and electrochemical capacitors.[1] Ferric oxide (α-Fe_2O_3, hematite) has become a very desirable material also to construct photoelectrochemical cells due its bandgap (E_g=~2.2eV) which allows utilization of a considerable portion of solar energy and stability in harsh chemical environments.[2] Non-toxicity, low cost and relative abundance of hematite on earth also add on its charm. Despite these exiting features, hematite suffers from poor conductivity, short photogenerated carrier life-time and a short hole diffusion length.[3] It has been demonstrated that poor charge-transport properties can be improved with nanostructured morphology which provides higher surface area.[4]

Several methodologies were employed to grow hematite nano-crystals including high-temperature based techniques such as pulsed layer deposition, catalyst-assisted chemical vapour deposition and thermal oxidation.[5] Techniques which required lower temperatures like solution based approaches; chemical precipitation, sol-gel, forced hydrolysis and hydrothermal synthesis were also applied.[1,6] Electrochemical synthesis is a simpler and cheaper alternative to produce semiconductor nanostructures. It is an efficient and environmental-friendly method where thin films on various substrates of any shape and size can be produced at relatively lower temperatures from aqueous media. Furthermore, by controlling deposition parameters like temperature, applied potential, precursor concentration; growth rate, film thickness, composition and morphology of the films can be modified [7–9] which are important factors for optimization of hole diffusion length or recombination rate in hematite structures.[2] In spite of its advantages, electrochemical synthesis requires strict control over applied potential and pH since Pourbaix diagram of Fe-water system shows possibility to obtain several different iron oxide phases.[10] It has been reported that magnetite (Fe_3O_4), goethite (α-FeOOH) and Lepidocrocite (γ-FeOOH) can be obtained by increasing the potential from -0.4 V to 1.0 V vs Ag(AgCl) from aqueous solutions containing $FeSO_4(NH_4)_2SO_4{\cdot}6H_2O$ and CH_3COOK (pH=6) at 90°C.[9] Both cathodic or anodic electrodepositions of α-Fe_2O_3 from aqueous solutions involve deposition of an iron oxyhydroxide phase followed by heat treatment to produce hematite phase.[11–14]

Hydrothermal approach also offers some advantages such as control over particle size and shape, homogeneity of the products and well-crystallized particles.[15] However, similar to electrodeposition, most cases of hydrothermal hematite synthesis involve formation of β-FeOOH precursor which is further dehydrated into α-Fe_2O_3 through calcinations or annealing.[1] Jia and Gao reported direct synthesis of single-crystalline α-Fe_2O_3 submicron-cubes via hydrothermal method at 180°C in the presence of surfactant with relatively long reaction times (16-36h).[16] Hence, in this study we combined benefits of hydrothermal synthesis with electrochemical deposition to obtain α-Fe_2O_3 films directly. It is demonstrated that synthesis of crystalline hematite nanosructures via single-step is possible with hydrothermal-electrochemical deposition (HED), owing to the high growth rate facilitated by high temperature.

Experimental

Iron(II) chloride hexahydrate ($FeCl_2.6H_2O$, 99 % purity) was

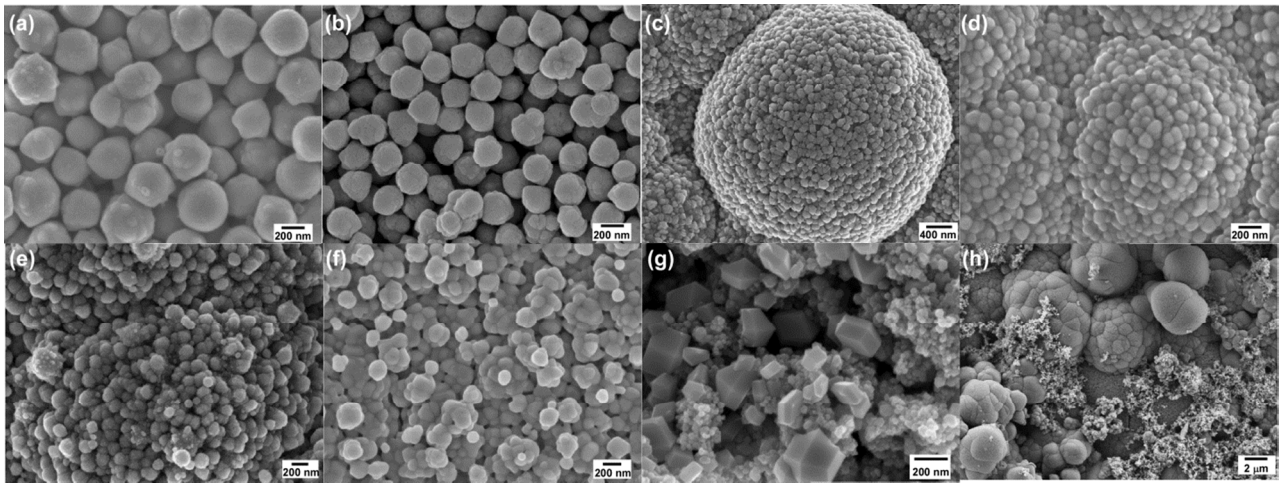

Fig.1 FE-SEM images of the films a) H1 as-deposited b) H1annealed c) H2 as-deposited d) H2 annealed e) H3 as-deposited f) H3 annealed g) H4 as-deposited h) H4 annealed.

Table 1 Deposition parameters for hydrothermal-electrochemical deposition at 130°C, 1.2 V vs Ag/AgCl(satd).

Film	[Fe2+]	[NaAc]	Deposition time
H1	0.02 M	-	8 min.
H2	0.02 M	0.08 M	8 min.
H3	0.05 M	-	8 min.
H4	0.05 M	0.1 M	8 min.

purchased from Sigma-Aldrich. Sodium acetate ($NaCH_3COO$, NaAc) was obtained from Merck. Indium Tin Oxide (ITO) ($\Omega < 5.0x10^{-4}$ ohm.cm (Rs<100 ohm/sq) was purchased from Teknoma Ltd. Izmir, Turkey and Fluorine doped tin oxide (FTO) was obtained from Solaronix SA. Double distilled, high purity water was used from Milli-Q water (Millipore) system. The depositions were performed in a hydrothermal glass reactor (100 ml, Büchiglasuster, picoclave) at constant potential at 130°C. The reference electrode was Ag/AgCl saturated with KCl (Corr Instruments, S/N P11092) whereas Pt wire served as counter electrode. Both acidic and neutral plating solutions were used for the anodic depositions at 1.2 V (vs Ag/AgCl(satd)).[13] Acidic plating solution contained 0.02 M $FeCl_2$ (pH~ 3.8) and neutral plating solution consisted of 0.02 M $FeCl_2$ and 0.08 M $NaCH_3COO$ (pH~6.2-6.8). The films were annealed at 520°C for 30 minutes. Reaction parameters are summarized in Table 1. The crystal structure and crystallinity of the thin films were analyzed by Bruker D8 Advance with DaVinci X-ray diffractometer (XRD). ZEISS Ultraplus Field Emission Scanning Electron Microscope (FE-SEM) was used to study the surface morphology of the samples.

Raman scattering experiments were carried out using a Renishaw Raman Microscope system at room temperature. Before conducting any measurements, the instrument was calibrated using an internal Si sample, which was measured at a Raman shift of 520 cm^{-1}. A 633 nm laser beam was focused on the samples. Phase transformations from FeO to Fe_3O_4, from Fe_3O_4 directly to α-Fe_2O_3 (martitization)[17] and from Fe_3O_4 first to γ-Fe_2O_3 then to α-Fe_2O_3[18] are reported for iron oxide films during Raman scattering at high laser powers. Hence sacrificial films were first excited at different laser powers to determine a threshold power so that no phase transformations take place and high enough power for reasonable signal-to noise ratio. At 0.12 mW signal intensity was very low and a laser power of 1.2 mW was determined to be a safe limit with no change in the observed spectra and high intensity signals. Spectra were taken over a range from wavenumbers 200 cm^{-1} to 1500 cm^{-1}. The acquisition time was 10 s to 30 s.

Diffuse reflectance spectra of the investigated samples were performed using a Shimadzu UV–vis–NIR 3600 spectrophotometer using integrating sphere attachments. Photoelectrochemical analyses were performed with Bio-Logic VSP model Potentiostat/Galvanostat system. The current-voltage (I-V) characteristics of the electrodes were measured under amplitude modulated-light illumination with a 300 W Xenon arc lamp (Oriel, Stratford, CT) with the 3 electrode cell system in an aqueous solution of 0.1 M NaOH. AM 1.5 air filter was used to mimic solar radiation with a power of 100 mW/cm^2.

Results and Discussion

We have investigated the effect of electrodeposition under hydrothermal conditions from both acidic and neutral deposition solutions on the structure and phase of iron oxide films. The hematite thin films deposited using the hydrothermal-electrochemical deposition range in colour from brown to deep red. It was observed that the films tend to adhere on FTO surface more strongly than ITO-coated glass. Hence, FTO was chosen as the substrate for the rest of the study. Increasing precursor concentration and high pH enhances adherence of iron oxide on the substrates. Figure 1 shows FE-SEM images of pristine and annealed films deposited at 130°C and ~ 2 bar. FE-SEM study showed that the pristine film prepared from an aqueous bath containing 0.02 M $FeCl_2$ (pH=3.8) with anodic electrodeposition, H1, is composed of monodisperse almost-spherical particles of around 300-400 nm which preserved their size and morphology after annealing (Figure 1a-b). With increasing the concentration of Fe^{2+} from 0.02 to 0.05 M, H3, the spherical shape develops into more like polyhedra and a high polydispersity in size is (80-150 nm) observed (Figure 1e). Although there are still particles

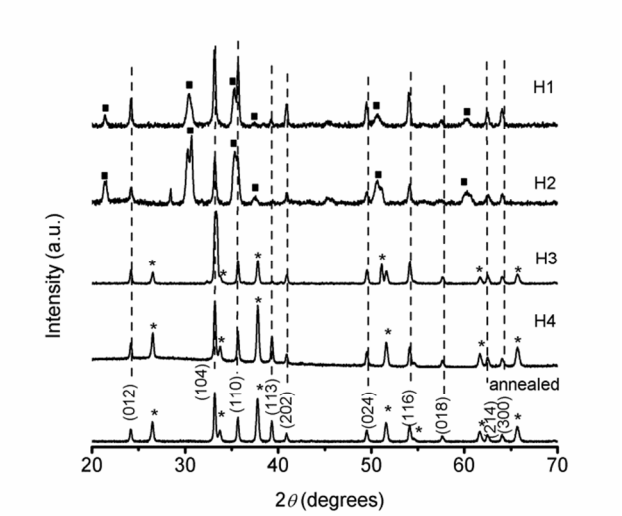

Fig.2 XRD profiles of the hematite films electrodeposited at 130°C, ~2 bar. The following symbols represent reflections associated with ∎ ITO(JCDPDS card No. 89-4597) and * SnO2 (JCDPDS card No. 41-1445).

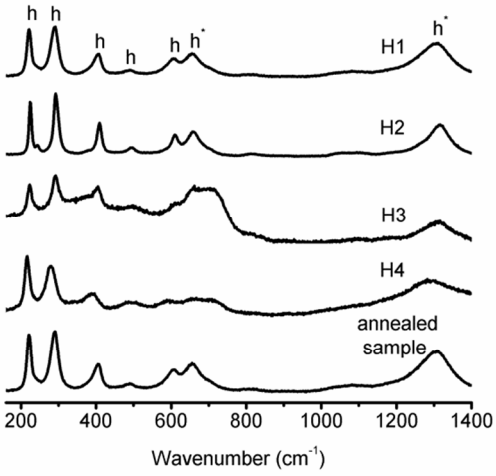

Fig.3 Raman spectra of the hematite films electrodeposited at 130°C, ~2 bar.

with smaller sizes (~50 nm), mostly larger aggregates of varying sizes are present after annealing (Figure 1f). Nano-iron oxide particles prepared from neutral deposition bath, H2, exhibit higher polydispersity than its counterpart which prepared from acidic deposition bath and distortion from spherical morphology (Figure 1c). Nanoparticles with diameters of 50-100 nm are observed to form large, spherical aggregates on the order of micrometers. Size and morphology are preserved after annealing (Figure 1d). When Fe^{2+} concentration was increased from 0.02 to 0.05 M (and corresponding [$NaCH_3COOH$]), H4, spherical nanoparticles with diameters ~50 nm and well-faceted polyhedra with a broad range of particle sizes form together (Figure 1g). After annealing, increase in average diameter of spherical nanoparticles to around 100 nm and formation of micrometer sized aggregates are observed (Figure 1h). In addition, polyhedral particles seem to have disappeared.

The anodic deposition of FeOOH films from ferrous sulfate solutions with varying pH was introduced by Cohen and Leibenguth in 1972.[12] The electrodeposited FeOOH films were then converted to hematite phase by annealing. Cohen and Leibenguth used ammonium sulfate/ammonium or boric acid/sodium borate to stabilize Fe^{2+} ions in neutral solution.[12] Spray and Choi modified the neutral deposition bath reported by Cohen and Leibenguth via replacing ammonium sulfate/ammonium or boric acid/sodium borate with NH_4Cl, and compared the photoelectrochemical properties of the products with that of the films obtained by anodic electrodeposition from acidic bath.[13] In this study, $NaCH_3COO$ was chosen for electrodeposition was carried out otherwise identical conditions as the depositions in acidic solution. The anodic deposition condition used in this study results in oxidation of Fe^{2+} ions to Fe^{3+} ions (eqn 1), which is followed by precipitation of Fe^{3+} ions as amorphous ferric oxyhydroxide due to the limited solubility of Fe^{3+} ions in the plating solution ($[Fe^{3+}] \approx 1\times10^{-7}$ at pH 4.1) (eqn 2);[13,9]

$$Fe^{2+} \rightarrow Fe^{3+} + 2e^- \quad (1)$$

$$Fe^{3+} + 2H_2O \rightarrow FeOOH + 3H^+ \quad (2)$$

Hence, it is expected that as-deposited films contain amorphous ferric oxyhydroxide which is converted to crystalline α-Fe_2O_3 upon annealing as reported before.[12,13] To identify the structure and phases of the obtained films, XRD was employed (Figure 2). XRD patterns of the as-synthesized films revealed peaks with highest intensities at 2Θ= 24°, 33°, and 35° which can be indexed to (012), (104) and (110) reflections of crystalline, Rhombohedral α-Fe_2O_3, hematite structure {JCPDS card No. 86-0550} even before the annealing step without any other phase being detected (Figure 2). The patterns exhibit an intensity distribution corresponding to the standard polycrystalline hematite structure, where the crystallites are randomly oriented. Moreover, crystallinity of the films improves with no accompanying compositional changes after annealing (Figure 2).

To further evaluate purity of hematite phase, Raman spectroscopy was used. Hematite belongs to the D^6_{3d} space group and seven transitions are expected in the Raman spectrum[17,19,20]. Two A_{1g} modes at 225 and 498 cm^{-1} and five E_g modes at 247, 293, 299, 412 and 613 cm^{-1} are expected. Raman spectrum of the as-synthesized films at 130 °C exhibit major peaks at 226, 247, 296, 411, and 615 cm^{-1} with 226 and 296 cm^{-1} being strongest all correspond well to α- Fe_2O_3 peaks (Figure 3). In addition to these peaks, modes around ~660 cm^{-1} and ~1320 cm^{-1} were present in all hematite Raman spectra obtained in the whole study. The 660 cm^{-1} mode is present in several published hematite spectra and it is either assigned to magnetite/wüstite (FeO) impurity or considered as characteristics of hematite and assigned to a disorder phase.[21,22,23] There is no evidence of any other iron oxide phase in the XRD diagrams of (Figure 2). Lack of evidence for presence of impurity phase suggests 660 cm^{-1} peak is related to hematite phase which has been ascribed to disorder in the crystal lattice and the breaking of symmetry upon crystallization.[21] The mode around 1320 cm^{-1} has been suggested to be an overtone of the peak at 660 cm^{-1}.[21] It was also ascribed to a two-magnon scattering including magnon-magnon interactions of antiferromagnetic hematite.[17] There are also additional peaks around 820 and 1050–1100 cm^{-1}. They are reported to exist in the

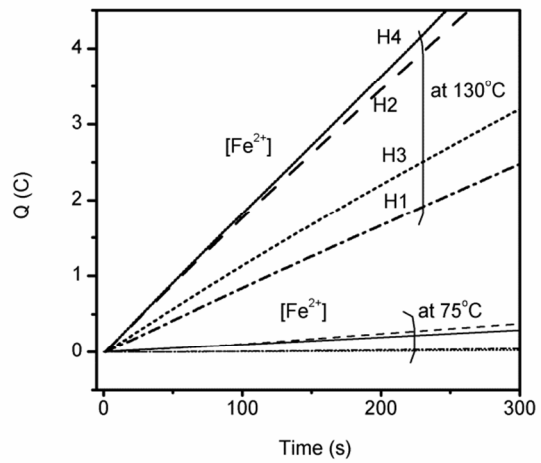

Fig. 4 Effect of initial $[Fe^{2+}]$, pH and temperature on electrodeposition rate.

xx polarized hematite spectra.[19] Hence, Raman spectroscopy data (Figure 3) together with XRD (Figure 2) demonstrates hematite phase forms directly with hydrothermal-electrochemical deposition at 130°C. This behaviour is contradictive to expected amorphous ferric oxyhydroxide (γ-FeOOH, as stated above) [12,13] or goethite[24] formation with anodic electrodeposition under ambient conditions and moderate temperatures. An example Raman spectrum for one of the annealed films is also provided in Figure 3.

Cohen and coworkers carried out the anodic deposition from ferrous sulfate solutions in neutral medium (pH varying between 6.6 and 8) and studied reaction kinetics.[12] They have shown that the deposition rate increases both with pH and $[Fe^{2+}]$. Leibenguth and Cohen discussed that deposition proceeds through diffusion and oxidation of ferrous hydroxyl complex and the formation of FeOOH instead of Fe_2O_3 depends on how fast ions are transferred to the anode. They proposed FeOOH forms rather than Fe_2O_3 owing to the fact that OH^- ions migrate easier than Fe^{+2} ions because of their smaller positive charge. The fact that α-Fe_2O_3 phase is obtained directly from both acidic and neutral HED suggests temperature effect rather than OH^- ion concentration has a major role. Figure 4 shows charge vs. time plot for depositions with varying parameters such as temperature, pH and initial $[Fe^{2+}]$. (Electrodeposition at 75°C was also carried out under identical conditions.) It can be seen that deposition rate increases with concentration (H1 ($[Fe^{2+}]$=0.02 M) and H3 ($[Fe^{2+}]$=0.05 M) at pH 3.8); H2 ($[Fe^{2+}]$=0.02 M) H4 ($[Fe^{2+}]$=0.05 M) at pH ~6.4) and pH (when H1 is compared with H2 and H3 is compared with H4) in accordance with what is reported by Leibenguth and Cohen. Moreover, the deposition rate increases much more effectively when temperature is increased from 75°C to 130°C while all other parameters are kept constant (Figure 4). Growth of hematite can be explained by the reaction;

$$2\,Fe^{2+} + 3H_2O \rightarrow Fe_2O_3 + 6H^+ + 2e^- \quad (3)$$

with the following equilibrium potential at 25°C calculated by using tabulated thermodynamic values for chemical species and Nerst equation;

$$E = 0.728 - 0.177pH - 0.0592\log[Fe^{2+}] \quad (4)$$

which results in thermodynamic potentials of -0.734 V for $[Fe^{2+}]$=0.02 M and -0.75 V for $[Fe^{2+}]$=0.05 M at 130°C, pH=6.4, and -0,112 V for $[Fe^{2+}]$=0.02 M and -0.128 V for $[Fe^{2+}]$=0.05 M at 130°C, pH=3.8. Taking the fact that a high overpotential is applied during deposition also into consideration, formation of hematite phase directly at high temperature might be explained by higher reaction kinetics.

Hematite nanoparticles are useful for various applications such as the anode of photoelectrochemical cells for water splitting, detection electrode for gas sensors, the positive electrode for Li-ion batteries and photodegradation of dyes may be promising.[25–27] We have evaluated the optical and photo-electrochemical performances of the films after post-annealing at 520°C except H1, since H1 did not adhere onto the substrate very effectively. The optical absorbance spectra of the films (Figure 5a) exhibit two broad absorption bands centered at around 345 nm and 514 nm. These bands are slightly blue shifted from the reported absorption bands of hematite which are normally observed at around 400 and 530 nm.[28,29,30] The degree of change of the peak positions is reported to depend on the shape and size of the particles.[27] Hence, the shift can be attributed to size quantization of the hematite nano-particles. The band at lower wavelength can be attributed to $^6A_1 \rightarrow {}^4E$ and $^6A_1 \rightarrow {}^4E$, ligand field transitions of Fe^{3+}.[28,27] The low energy band is ascribed to $^6A_1 \rightarrow {}^4T_2$ ligand field transition of Fe^{3+}.[29,27] In addition, two charge- transfer transitions accompany these processes; a direct transition corresponding to the ligand-metal transfer ($O_2 \rightarrow Fe^{3+}$) at higher energy and an indirect transition at higher wavelength from the metal-metal transfer.[27,31]

PEC performances of annealed α-Fe_2O_3 electrodes were measured under amplitude modulated 1 sun illumination at 1.1 V vs NHE in 1 M NaOH (Figure5b) at a lower than theoretical water oxidation potential (Eqn 3; E^o (O_2/H_2O) = 1.23 V vs NHE at pH 13.5). The anodic nature of the photocurrent produced suggests n-type behavior for all of the films and the responses are quite stable with no sign of photocorrosion. The net photocurrent densities of the films are 11.3, 11.4, and 23.6 μA/cm^2, respectively for H2, H3 and H4. The photoresponse of film prepared from a highly concentrated, neutral bath (H4) is almost twice of the responses of the other films. In addition the photocurrent switching (ON/OFF) response of H4 is faster than both H2 and H3. Even though, H2 consists of smaller sized particles (Figure 1), which provide higher surface area and thereby beneficial to decrease recombination losses[13], H4 generates higher photocurrent than H2.

The difference in photoresponses of H2 and H4 can be attributable at least, in part, to higher Fe_2O_3 loading on H4. As discussed above, deposition rate is increases with increasing $[Fe^{++}]$. Hence, higher amount of hematite should be deposited from more concentrated deposition bath at a given time which would result in increased number of generated electron-hole pairs that can contribute to photocurrent generation for H4. On the other hand, similar deposition rate for H3 and H4 (Figure 4) suggests similar Fe_2O_3 loading for these films. In addition, as can be seen in Figure 5a, H3 displays higher photon absorption. Therefore, H3 was expected to generate higher photocurrent. However, H3 is composed of 300-400 nm sized polyhedral

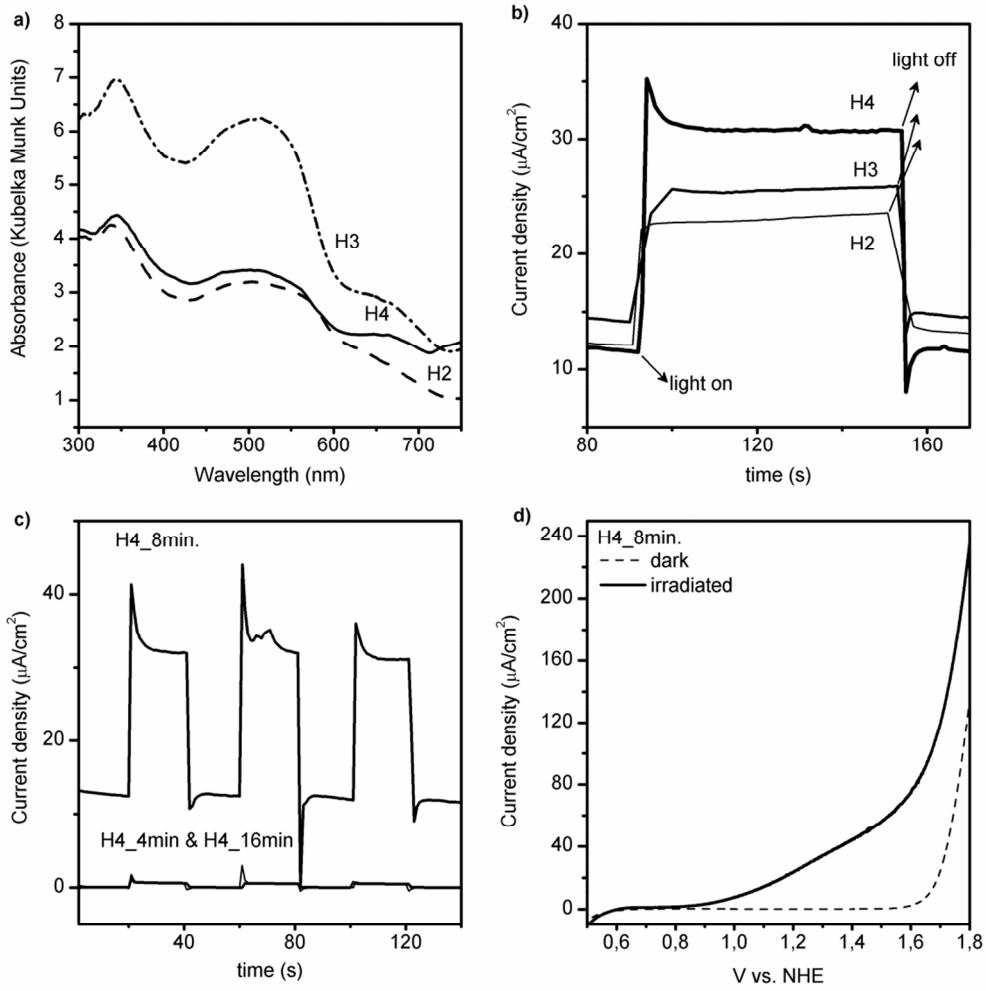

Fig. 5 a) UV/visible light absorption spectra of hematite films electrodeposited at 130°C, ~2 bar, b) The photocurrent responses of the hematite films at 1.1 V vs. NHE under amplitude modulated illumination, c) The photocurrent responses of H4 with varying deposition time at 1.1 V vs. NHE under amplitude modulated illumination, d) Photocurrent–voltage (J–V) curves of H4_8min under dark and illumination at 100 mW/cm^2 (AM 1.5 air filter)..

whereas spherical nanoparticles of around 100 nm are observed for H4. Smaller particle size, hence higher surface area of H4 allows more holes to reach the hematite/electrolyte interface which reduces recombination losses[13] and results in higher photocurrent generation.

As an effort to optimize obtained photoresponse, films were prepared from neutral, concentrated (0.05M Fe^{2+}) deposition bath with different deposition times (H4_4min, H4_16min). PEC performances were measured under identical conditions.

Photocurrent density increased ~40-fold as the deposition time increased from 4 min. (0.66 μA/cm^2) to 8 min. (23.6 μA/cm^2) (Figure 5c). Analyzing FE-SEM images implies that surface morphologies of the films are very similar with nanometer-sized spherical particles and micrometer-sized aggregates (Figure 1 and 6). The thickness of the samples was measured by taking cross sectional FE-SEM images. Films deposited for 4 and 8 min. resulted in films with average thickness of 1.2 and 1.33 μm calculated from cross-sectional FE-SEM images (Figure 6). The increase in the photoresponse from 4 to 8 min. can be attributed to increase in the number of electron-hole pairs due to the presence of additional photoactive oxide in the thicker film. After 16 min. of deposition, photocurrent density generated decreased to around 0.7 μA/cm^2 similar to H4_4min. It is reported that when the thickness of the hematite film reaches beyond 2.6 μm, the distance that holes would travel to reach the Fe_2O_3/electrolyte interface is increased which results in higher recombination probability.[32] Increased hole-diffusion length together with a reduced photon penetration for a thicker film[29] might account for decrease in produced photocurrent with H4_16min.

The photocurrent–voltage (J–V) pattern of H4 measured under identical conditions is shown in (Figure5d). The onset potential for H4 is calculated by extrapolating the linear portion of the J–V curve to zero current from where current densities range from 15 to 60 μA/cm^2. The photocurrent onset potential calculated to be 0.96 V vs RHE. After onset, photocurrent shows two separated potential regions.[29] In the first region photocurrent increases to

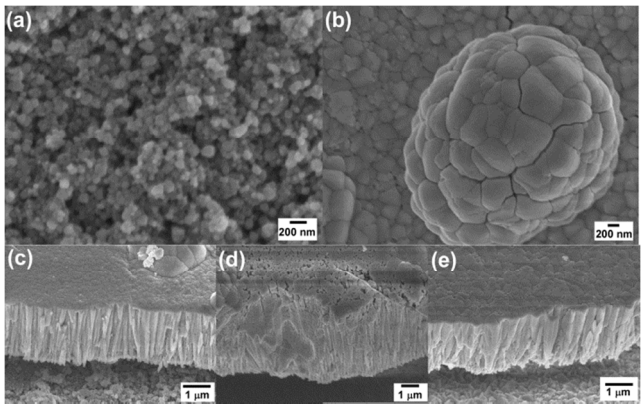

Fig.6 FE-SEM images of a) H4_4min. b) H4_16min. and cross-sectional FE-SEM images of c) H4_4min. d) H4_8min. e) H4_16min.

reach 26.5 μA/cm^2 at 1.23 V vs NHE and 72.75 μA/cm^2 at 1.6 V vs NHE. This region corresponds to where four-electron water oxidation reaction takes place (eqn 5). From 1.6 V to 1.8 V (where photocurrent density reaches 102 μA/cm^2) is the second region where also two-electron water oxidation (eqn 6) takes place.

$$2H_2O \rightarrow O_2 + 4H^+ + 4e^-,\ E^o\ (O_2/H_2O) = 1.23\ V\ vs\ NHE \quad (5)$$

$$2H_2O \rightarrow H_2O_2 + 2H^+ + 2e^-,\ E^o\ (O_2/H_2O) = 1.776\ V\ vs\ NHE \quad (6)$$

Preparation of doped hematite films to enhance the PEC performances by presented hydrothermal-electrochemical deposition technique and post-surface modifications to reduce surface recombination probability are currently under study.

Conclusions

Hydrothermal-electrodeposition was successfully employed to produce α-Fe_2O_3 and the effect of electrodeposition temperature on the structure and phase of iron oxide films was studied. In line with the literature, potensiostatic electrodeposition at ambient temperatures such as 75°C results in formation of amorphous iron oxide particles which can be converted to hematite (α-Fe_2O_3) upon thermal treatment. Combining electrochemistry with advantages of hydrothermal synthesis allows growth of crystalline α-Fe_2O_3 phase directly at a single step on the conducting glass. It is demonstrated that regardless of pH, growth time and presence of additives (CH_3COO^-), hematite crystals are obtained with anodic HED most probably due to increased reaction kinetics at high temperature. Thickness of the films can be adjusted with growth time and pH is found to be effective on both reaction kinetics and the final particle size. Higher pH and higher precursor concentration favour increased deposition rate in line with the observations of Cohen and Leibenguth and smaller particle size.

Photoelectrochemical studies demonstrated that higher performance can be obtained with the films prepared via HED than films electrodeposited at lower temperatures. Net photocurrent density of the 23.6 μA/cm^2 is obtained in 0.1 M NaOH under 1 sun conditions at 1.23 V vs NHE with the film prepared from a bath containing 0.05 M $FeCl_2$ and 0.1 M $NaCH_3COOH$ via hydrothermal-electrodeposition with a photocurrent onset potential of 0.96 V vs NHE.

Acknowledgements

Authors thank Koc University Faculty of Science for financial support. Authors would also like to express gratitude to Turkish Ministry of Development for the financial support provided for the establishment of Koc University Surface Science and Technology Center (KUYTAM). A special thank is for Dr. Barıs Yagci for his help in obtaining FE-SEM images and Raman spectra.

Notes and references

[a] *Graduate School of Science and Engineering, Koc University, Sariyer 34450 Istanbul,Turkey. Fax: +90-(212)-338 1559; Tel: +90-(212)-338 1339; E-mail: ugunal@ku.edu.tr*
[b] *Koc University, Chemistry Department, Sariyer, 34450 Istanbul, Turkey*
[c] *Koc University Surface Science and Technology Center (KUYTAM), Sariyer, 34450 Istanbul, Turkey*

1 M. Mohapatra and S. And and, *Int. J. Eng. Sci. Technol.*, 2010, **2**, 127–146.
2 D. K. Bora, A. Braun and E. C. Constable, *Energy Environ. Sci.*, 2013, **6**, 407.
3 M. J. Katz, S. C. Riha, N. C. Jeong, A. B. F. Martinson, O. K. Farha and J. T. Hupp, *Coord. Chem. Rev.*, 2012, **256**, 2521–2529.
4 C. I. Kay A Grätzel M., *J. Am. Chem. Soc.*, 2006, **128**, 15714–21.
5 D. A. Wheeler, G. Wang, Y. Ling, Y. Li and J. Z. Zhang, *Energy Environ. Sci.*, 2012, **5**, 6682.
6 L. Guo, S. Ida, H. Hagiwara, T. Daio and T. Ishihara, *Colloids Surfaces A Physicochem. Eng. Asp.*, 2014, **451**, 136–143.
7 D. Pradhan and K. T. Leung, *Langmuir*, 2008, **24**, 9707–16.
8 S. Lee, S. K. Park, C. R. Park, J. Y. Lee, J. Park and Y. R. Do, *J. Phys. Chem. C.*, 2007, 11793–11801.
9 L. Martinez, D. Leinen, F. Martín, M. Gabas, J. R. Ramos-Barrado, E. Quagliata and E. A. Dalchiele, *J. Electrochem. Soc.*, 2007, **154**, D126.
10 M. Pourbaix, *Atlas of Electrochemical Equilibria in Aqueous Solutionsi 2nd Edition, National Association of Corrosion Engineers, Houston, TX*, 1974.
11 R. Schrebler, K. Bello, F. Vera, P. Cury, E. Muñoz, R. del Río, H. Gómez Meier, R. Córdova and E. A. Dalchiele, *Electrochem. Solid-State Lett.*, 2006, **9**, C110.
12 J.-L. Leibenguth and M. Cohen, *J. Electrochem. Soc.*, 1972, **119**, 987.
13 R. L. Spray and K.-S. Choi, *Chem. Mater.*, 2009, **21**, 3701–3709.
14 S. Jiao, L. Xu, K. Hu, J. Li, S. Gao and D. Xu, *J. Phys. Chem. C*, 2010, **114**, 269–273.
15 Z. Jing and S. Wu, *Mater. Lett.*, 2004, **58**, 3637–3640.
16 B. Jia and L. Gao, *Cryst. Growth Des.*, 2008, **8**, 1372–1376.
17 D.L.A. de Faria, S. V. Silva and M. T. de Oliveria, *J. Raman Spectrosc.*, 1997, **28**, 873–878.
18 Y.-S. Li, J. S. Church and A. L. Woodhead, *J. Magn. Magn. Mater.*, 2012, **324**, 1543–1550.
19 D. Bersani, P. P. Lottici and A. Montenero, *J. Raman Spectrosc.*, 1999, **30**, 355–360.
20 S. Das and M. J. Hendry, *Chem. Geol.*, 2011, **290**, 101–108.
21 B. M. Klahr, A. B. F. Martinson and T. W. Hamann, *Langmuir*, 2011, **27**, 461–8.
22 J. A. Glasscock, P. R. F. Barnes, I. C. Plumb, A. Bendavid and P. J. Martin, *Thin Solid Films*, 2008, **516**, 1716–1724.
23 I. Cesar, K. Sivula, A. Kay, R. Zboril and M. Gra, *J. Phys. Chem. C*, 2009, **113**, 772–782.
24 S. Jiao, L. Xu, K. Hu, J. Li, S. Gao and D. Xu, *J. Phys. Chem. C*, 2010, **114**, 269–273.

25 L. Guo, S. Ida, A. Takashiba, T. Daio, N. Teramae and T. Ishihara, *New J. Chem.*, 2014, **38**, 1392.

26 H. Liang, X. Xu, W. Chen, B. Xu and Z. Wang, *CrystEngComm*, 2014, **16**, 959.

27 W. Zhu, X. Cui, X. Liu, L. Zhang, J.-Q. Huang, X. Piao and Q. Zhang, *Nanoscale Res. Lett.*, 2013, **8**, 2.

28 P. Kumar, P. Sharma, R. Shrivastav, S. Dass and V. R. Satsangi, *Int. J. Hydrogen Energy*, 2011, **36**, 2777–2784.

29 A. Bak, W. Choi and H. Park, *Appl. Catal. B*, 2011, **110**, 207–215.

30 S. K. Mohapatra, S. E. John, S. Banerjee and M. Misra, *Chem. Mater.*, 2009, **21**, 3048–3055.

31 T. J. Latempa, X. Feng, M. Paulose, C. A. Grimes, V. Uni, U. V Park and V. Pennsyl, *J. Phys. Chem. C*, 2009, **113**, 16293–16298.

32 A. Kleiman-Shwarsctein, M. N. Huda, A. Walsh, Y. Yan, G. D. Stucky, Y.-S. Hu, M. M. Al-Jassim and E. W. McFarland, *Chem. Mater.*, 2010, **22**, 510–517.